

Solar Channel Calibration Using Desert Targets in Australia: Application to the MTSAT-1R Visible Sensor

Hyung-Wook CHUN, Byung-Ju SOHN

School of Earth and Environmental Sciences, Seoul National University, Seoul, Korea

Do-Hyeong KIM, Myoung-Hwan AHN

Korea Meteorological Administration, Seoul, Korea

and

Mi-Lim OU

National Institute of Meteorological Research, Seoul, Korea

(Manuscript received 19 July 2011, in final form 26 December 2011)

Abstract

Focusing on the use of desert targets for solar channel calibration of geostationary satellites located in the west Pacific region, a desert target in Simpson Desert, Australia, was selected and used for the development of a calibration algorithm based upon radiative transfer modeling. The surface spectral reflectance required for radiative transfer calculation was obtained from the Moderate Resolution Imaging Spectroradiometer (MODIS)-bidirectional reflectance distribution functions after tuning against the Advanced Spaceborne Thermal Emission and Reflection Radiometer (ASTER) spectral data. Top of the atmosphere radiance simulations were conducted over the desert target, and comparisons with MODIS- and Sea-viewing Wide Field-of-view Sensor (SeaWiFS)-measured visible channel radiances revealed that the developed calibration method using the target over the Simpson Desert can be used to calibrate the geostationary visible channel within a 5% level of uncertainty. Application of the developed algorithm to Multi-Functional Transport Satellite (MTSAT-1R) visible channel measurements suggested that the MTSAT-1R operational calibration for the visible sensor appeared to be within a 5% error, but over the lower count value range.

1. Introduction

Visible channel measurements from meteorological satellites provide important meteorological and geophysical parameters, such as cloud and aerosol properties, and radiation budget parameters for the top of

the atmosphere (TOA) and surface. However, absolute radiometric calibrations are a prerequisite for obtaining accurate values for such parameters from visible channel measurements. In general, before satellite launch, preflight calibrations are performed in optical laboratories for absolute calibrations (e.g., Barnes et al. 1998). However, the sensor sensitivity may degrade during its multi-year operation due to many factors, such as extraterrestrial solar radiation, aging of sensor optics, and molecular outgassing of the instrument. Therefore, in-flight calibrations are necessary in order to assess the performance of the absolute calibration as well as to monitor sensor degradation. In-flight calibrations are

Corresponding author: B. J. Sohn, School of Earth and Environmental Sciences, Seoul National University, NS80, Seoul, 151-747, Korea
E-mail: sohn@snu.ac.kr

©2012, Meteorological Society of Japan

particularly important for geostationary weather satellites that are generally not equipped with an onboard calibration system for the visible sensor.

In-flight vicarious calibration methods can be of three types: (1) cross-satellite calibration, (2) airborne calibration campaign, and (3) stable Earth target approach with radiative transfer modeling (Govaerts et al. 2004). The cross-satellite calibration method is widely used to monitor the trends of a target sensor relative to a reference sensor, even though the target sensor is generally different from the reference sensor in spectral range and response function (e.g., Cao et al. 2008; Minnis et al. 2008). In general, the effects of spectral differences, angular reflectivities, and different footprint sizes must be taken into account during the intercalibration, which can be a difficult task. Spatially extensive hyperspectral imageries from airborne sensors can be more directly used to perform vicarious radiometric calibration for other sensors in similar spectral ranges (Teillet et al. 2007). Airborne campaigns are useful for evaluating the accuracy of a calibration; however, monitoring the long-term drift of any sensor can prove to be quite expensive. Comparatively, calibrations based on the stable Earth target approach with radiative transfer modeling are affordable and allow us to monitor sensor degradation with reasonable accuracy for the determined absolute calibration coefficients (Govaerts et al. 2004). However, this simulation approach requires accurate radiative transfer modeling of the atmosphere as well as the surface.

This study focuses on vicarious calibration using radiative transfer modeling for which bright desert targets are widely used (Vermote and Saleous 2006; Govaerts and Clerici 2004; Govaerts et al. 2004; Miesch et al. 2003; Cosnefroy et al. 1996). Bright desert targets tend to be temporally invariant and spatially stable, and therefore, radiative transfer modeling is relatively easier once the characterization of the surface radiative properties is accurately conducted. Furthermore, since the atmospheric contribution to the TOA radiance is relatively small over the dry desert area compared to the surface contribution over the bright surface, the fractional uncertainty ratio induced by the incorrect atmospheric contribution can be minimized over the desert area.

Although the desert target approach is useful, developments in this area have been mostly limited to bright deserts located at low latitudes, such as the Sahara and Arabian deserts. Few efforts have been made using an Australian desert target for calibration (e.g., Mitchell et al. 1997), and the Australian desert has never been used for the operational calibration of geostationary satellites located over the East Asia–West Pacific region, partly

because deserts are located at higher latitudes.

Calibrating the visible sensor of the geostationary Multi-Functional Transport Satellite (MTSAT)-1R located at 140°E with the aid of radiative transfer modeling, we selected proper desert targets in the East Asia and Australian regions using long-term surface parameter data obtained from satellite measurements. Then, we developed a vicarious calibration method based on surface characterization and radiative transfer modeling over the selected desert target. The developed method was then used to evaluate the operational calibration status of the MTSAT-1R visible sensor.

2. Methodology and data sets

The procedures for calibrating the visible channel sensors aboard the geostationary satellite located in the East Asia–West Pacific region are outlined in Fig. 1. First, targets showing stable behaviors in both time and space were selected by analyzing multi-year bidirectional reflectance distribution function (BRDF) data derived from Terra/Aqua Moderate Resolution Imaging Spectroradiometer (MODIS) measurements. Once the desert targets were selected, MODIS BRDF parameters were combined with National Aeronautics and Space Administration (NASA) Jet Propulsion Laboratory (JPL) Advanced Spaceborne Thermal Emission and Reflection Radiometer (ASTER) spectral albedo library data to obtain the spectral BRDFs of the chosen desert targets for a given geometric angle and observation time of the satellite. Then, for clear-sky scenes, characterized surface optical properties were used with atmospheric profiles as inputs to a radiative transfer model for the simulation of radiance at the satellite's altitude. Simulated radiances were then compared against measured radiances for the reference satellites (MODIS) to estimate the uncertainty level. Final sensor calibration was performed by comparing simulated radiances for the target sensor to observed digital counts. The summary of data used is given in Table 1, and detailed information about the data sets used for the calibration procedures is provided in the following subsections.

2.1 Surface parameters

a. MODIS BRDF

Since surface reflectance varies with the positions of the sun and satellite, the BRDF of the target surface was required for radiative transfer calculation. In this study, MODIS-derived BRDFs given at 7 spectral channels (ranging from 460 nm to 2,150 nm) were used as a basis to determine BRDFs at 2.5-nm intervals over the spectral range from 500 nm to 900 nm

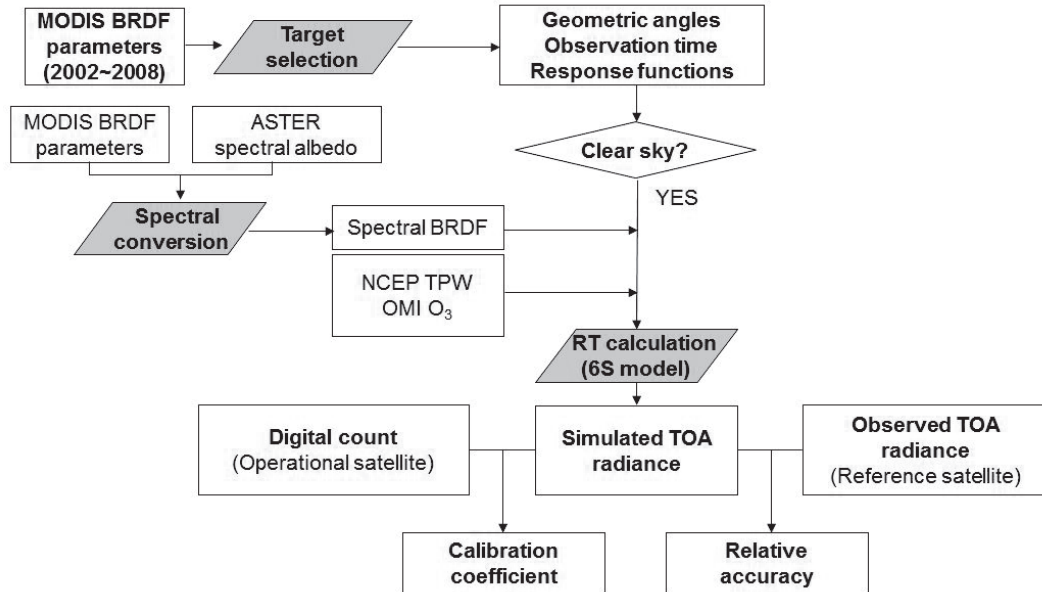


Fig. 1. Schematic of the calibration algorithm using the desert target. Detailed explanation is provided in the text. Shaded parallelogram boxes represent the processes discussed in detail in the text.

in conjunction with the ASTER spectral library. It is worth mentioning that the use of ASTER spectral library is due to the lack of ground observations of spectral albedos over the study region. In order to obtain MODIS BRDFs at 7 spectral bands, a composite of surface reflectances at an 8-day interval with a 0.05° spatial resolution was first made from all available cloud-free atmosphere-corrected reflectances over the previous 16-day period. Then, BRDFs, given as a function of solar zenith angle and satellite viewing angle, were obtained by minimizing the total variance differences between semi-empirical, kernel-driven BRDF model results and the composite of clear-sky reflectance over 7 MODIS visible bands.

Details of the MODIS BRDF algorithm are found in Lucht et al. (2000), and we provide a brief explanation about the algorithm here. The theoretical basis of the kernel-driven model is that the land surface reflectance $R_i(\theta, \vartheta, \phi)$ (at i th MODIS channel, solar zenith angle θ , satellite viewing zenith angle ϑ , and relative azimuth angle ϕ) can be modeled as a sum of three kernels representing basic scattering types: (1) isotropic scattering f_i^{iso} , (2) radiative transfer-type volumetric scattering from horizontally homogeneous leaf canopies $f_i^{vol} K_{vol}(\theta, \vartheta, \phi)$, and (3) geometric-optical surface scattering from scenes containing 3-D objects

$f_i^{geo} K_{geo}(\theta, \vartheta, \phi)$, i.e.:

$$R_i(\theta, \vartheta, \phi) = f_i^{iso} + f_i^{vol} K_{vol}(\theta, \vartheta, \phi) + f_i^{geo} K_{geo}(\theta, \vartheta, \phi) \quad (1)$$

where K is the model kernel and f is the BRDF parameter. Subscripts (or superscripts) 'iso', 'vol', and 'geo' represent isotropic, volume, and geometric-type scatterings, respectively. The three BRDF parameters (i.e. f_i^{iso} , f_i^{vol} , and f_i^{geo}) retrieved in an 8-day cycle were downloaded from the Land Processes Distributed Active Archive Center of the U.S. Geological Survey (<https://lpdaac.usgs.gov/>). For this study, collection 5 MODIS Terra and Aqua BRDF parameters and their associated quality flags are obtained from MCD43C1 and MCD43C2, respectively.

Two types of albedos obtained from MODIS BRDFs were used in this study, i.e., black-sky and white-sky albedos. The black-sky albedo is the reflectance associated with radiation coming from a direct light source within the hemisphere, whereas the white-sky albedo is the reflectance of diffused radiation coming from all directions in the hemisphere. The black-sky albedo is derived from integration of BRDF over the hemisphere (2π of solid angle), and detailed explanation regarding the black-sky albedo is deferred to Subsection 4.1

Table 1. Summary of used data.

Variable	Data source	Period	Spatial resolution
Radiance	MODIS/Terra	2005–2007	1 km
Radiance	SeaWiFS/SeaStar	2005–2007	4.5 km
Radiance	JAMI/MTSAT-1R	Nov. 2007–Jun. 2008	1 km
BRDF	MODIS/(Terra, Aqua)	2002–2008	0.05°
TPW	NCEP	2005–2008	2.5°
Ozone	OMI/Aura	2005–2008	1.0°

methodology. Target selection was made by examining the spatial and temporal behaviors of the white-sky albedo, which was obtained by integrating BRDFs over the hemisphere under the assumption that isotropic diffuse radiation was coming from all directions.

b. ASTER spectral surface reflectance

The ASTER library provides the spectral albedos for more than 2000 natural and man-made surface materials (Baldrige et al. 2009). ASTER data provide spectral albedos over the band from visible to thermal infrared wavelengths (400–15, 400 nm) for the given surface type. All available 41 soil types in the ASTER library were used in this study to convert narrow-band MODIS BRDF parameters over the selected desert targets to MTSAT-1R broadband parameters. The conversion method is provided in more detail in Section 4.

2.2 Atmospheric parameters

Since the algorithm employed radiative transfer calculations in the atmosphere, the specification of atmospheric thermodynamic conditions was necessary. However, we only specified total water vapor and ozone amounts because these were the two radiatively active gases in the visible spectral range of interest. Reanalysis data from the National Centers for Environmental Prediction (NCEP) were used to obtain the total water vapor amount (available 4 times daily at a 2.5° spatial resolution from <http://www.esrl.noaa.gov/psd/data/reanalysis/reanalysis.shtml>).

Ozone absorption was also counted by using the total ozone amount estimated by the Ozone Monitoring Instrument (OMI) onboard the Aura satellite. The OMI measures solar backscattered radiation in the visible and ultraviolet spectrum (<http://aura.gsfc.nasa.gov/instruments/omi.html>); backscattered radiation shorter than 340 nm in wavelength was used to retrieve the total ozone amount. The detailed OMI algorithm for estimating the ozone amount can be found in the

user's manual provided on the following Website: http://toms.gsfc.nasa.gov/version8/v8toms_atbd.pdf.

The total ozone amount per day, given with 1.0° spatial resolution, can be downloaded from <ftp://toms.gsfc.nasa.gov/pub/omi/data/ozone/>.

2.3 TOA radiances

The simulated TOA radiances at the three MODIS channels (640, 860, and 550 nm) were compared over the selected targets with MODIS-measured radiances in order to assess simulation accuracy. The MODIS sensor is well calibrated (Xiong and Barnes 2003), and can therefore be used as a reference for intercalibrating other satellite sensors carrying channels at similar spectral bands. MODIS radiance data (MOD021KM), geometric angle data (MOD03), and cloud mask data (MOD35) over the 2005–2007 period at 1-km resolution was used for this purpose.

Sea-viewing Wide Field-of-view Sensor (SeaWiFS) measurements were also considered for assessing the accuracy of the developed algorithm because the operational calibration of SeaWiFS is reported to be accurate (McClain et al. 2004). Among 8 SeaWiFS spectral channels ranging from 402 to 885 nm, radiance measurements at 555 nm, 670 nm, and 765-nm bands were examined. The global-area coverage (GAC) type SeaWiFS data, with a 4.5-km spatial resolution, are available from the NASA Ocean Color Website (<http://oceancolor.gsfc.nasa.gov/>). SeaWiFS radiance, related geometric angles, and cloud mask were extracted from GAC data using the SeaWiFS Data Analysis System (SeaDAS).

The Japanese Advanced Meteorological Imager (JAMI) onboard MTSAT-1R was chosen as a target sensor. JAMI measures radiances at 1 visible channel centered at 724 nm with a 1-km resolution (Japan Meteorological Agency 2003). By comparing the MTSAT-1R measured visible channel radiances with MODIS-based simulation results over the desert targets, we assessed the performance of the MTSAT-1R visible channel cal-

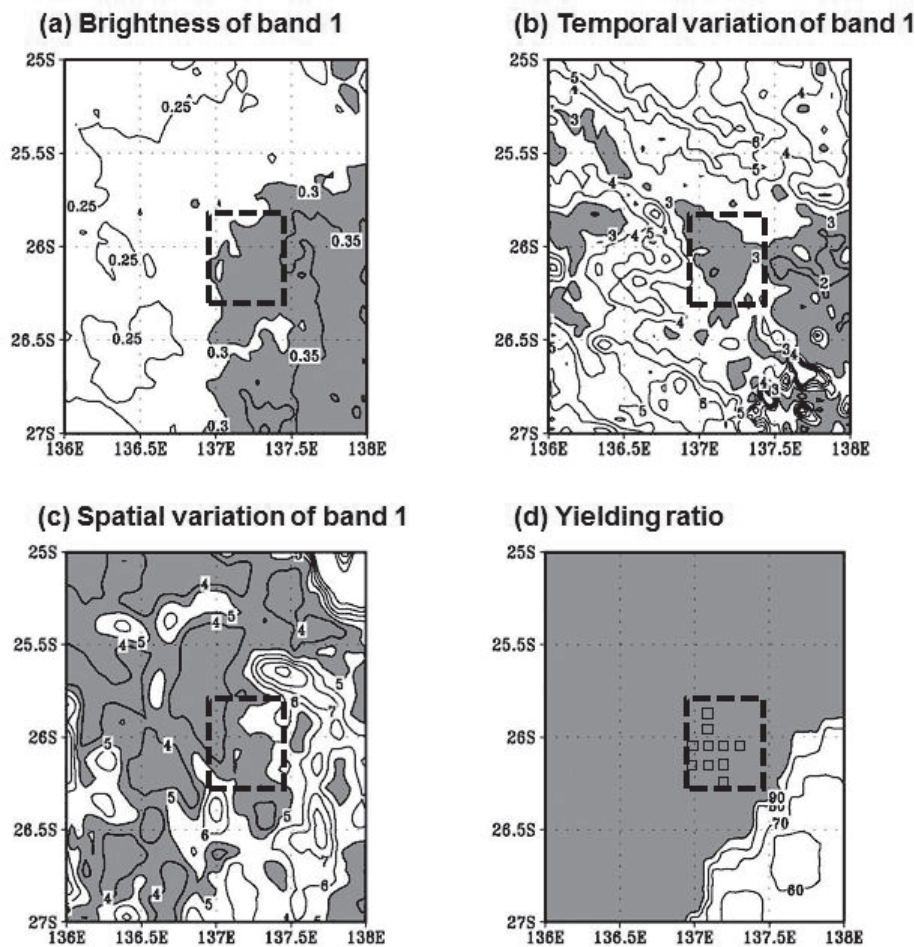


Fig. 2. Geographical distributions of (a) brightness (white-sky surface albedo), (b) temporal variation, and (c) spatial variation of the surface brightness for MODIS band 1 (640 nm) over the Simpson Desert in Australia. Also given is (d) yielding ratio expressing the data availability of MODIS BRDF parameters. The applied criteria for further analysis are 0.3, 3%, 5% and 95% in (a), (b), (c), and (d), respectively, and satisfying areas are shaded. Dashed box represents a selected calibration target, and small squares within the target box represent 10 sub-targets used for radiance simulations.

ibration during the period from November 2007 to June 2008. The clear-sky scenes of MTSAT-1R visible measurements were determined using a cloud detection algorithm developed by Chung et al. (2006).

3. Characteristics of selected desert target

Selecting calibration targets, we examined the magnitude, spatial uniformity, and temporal stability of the surface albedo over the Australian desert area. White-sky albedo, instead of surface reflectance, was used to examine the temporal and spatial characteristics of the

target surface. White-sky albedo is independent of the geometric angles of the sun and satellite, and can therefore be used to examine the variation caused by changes in surface conditions.

The surface brightness (i.e., the magnitude of white-sky albedo) was used to determine targets that could be potential calibration targets (Fig. 2a). Since the TOA radiance over the bright target areas was mainly controlled by the surface contribution, the relative error caused by incorrect specification of atmospheric conditions can be minimized when the surface characterization is properly

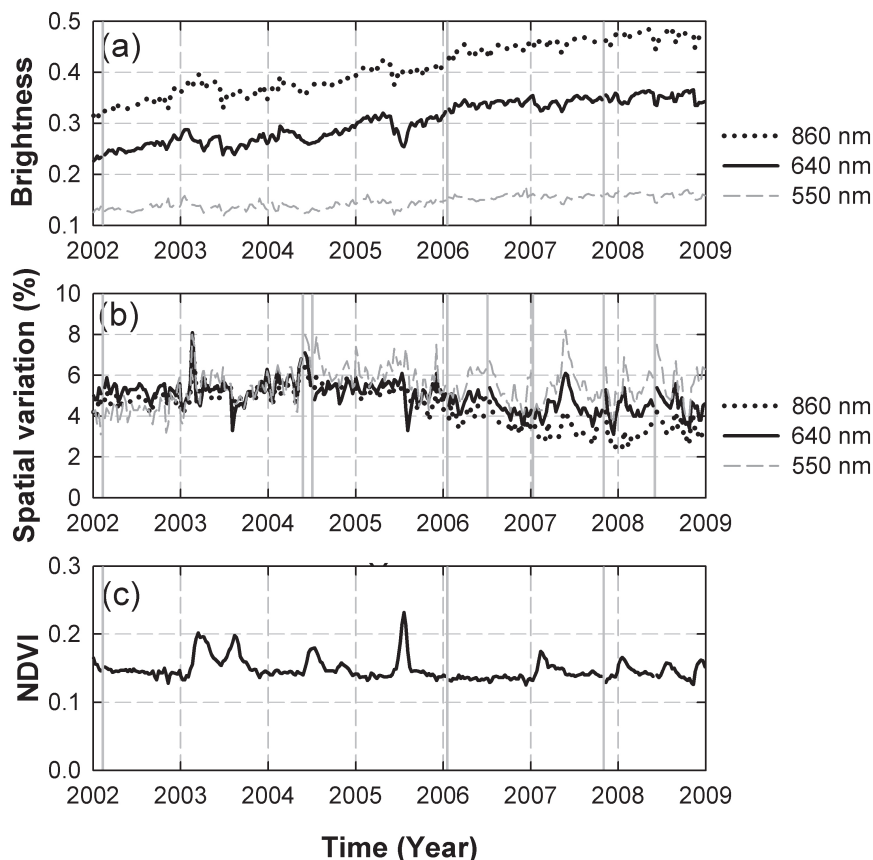


Fig. 3. Time series of (a) brightness, (b) spatial variation, and (c) NDVI at the center point of the selected calibration target. Data missing or low-quality BDRF data are expressed with vertical solid gray lines in each diagram.

conducted.

Temporal variations of white-sky albedo were examined to find more stable targets. These temporal variations were obtained by calculating the 7-year mean standard deviation, but normalized with the 7-year mean value over the 2002–2008 period (Fig. 2b). Spatial uniformity was checked to reduce the influence of possible navigation errors in the calibration by calculating the total variance of white-sky albedo within a moving 5×5 grid (about $20 \text{ km} \times 20 \text{ km}$) window (see Fig. 2c for the normalized percentage variance against the mean value). The normalized percentage variance is later used for selecting targets, in conjunction with other criteria.

In order to avoid targets contaminated by vegetation, we employed the Normalized Difference Vegetation Index (NDVI) determined from white-sky albedo at band 1 (640 nm) and band 2 (860 nm). MODIS white-sky albedos were used in this quality check only

if the MODIS BRDF quality flag was zero, which meant that the MODIS BRDF parameters were reliable under clear-sky conditions. The number of 8-day period data showing good quality (i.e., zero flag) for BRDF parameters during the 7-year period was counted in order to obtain the data yielding ratio; this is because TOA radiance simulation (and therefore, the calibration check) was only possible when the surface characterization was properly conducted.

Using the aforementioned surface parameters (i.e., brightness, temporal and spatial variation of white-sky albedo, and NDVI), desert areas in Australia were examined as a means to select calibration targets. Chinese deserts such as the Taklimakan, Jilin, and Gobi deserts were excluded because of their geographical locations—they are located mid-latitude and further west, inducing more uncertainties due to the longer optical path of the atmosphere and less reliable surface

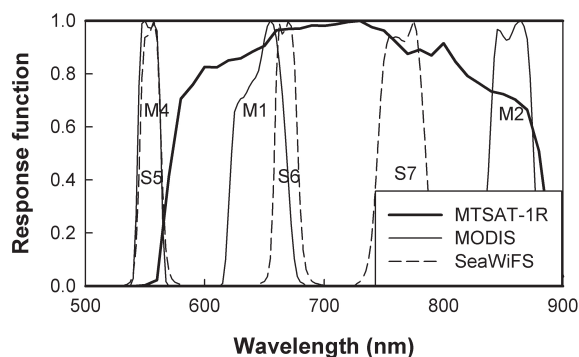


Fig. 4. The spectral response functions for the MODIS/Terra (thin solid lines), SeaWiFS/SeaStar (dashed lines), and JAMI/MTSAT-1R (thick solid line) solar channels. Channel numbers are also given after M (for MODIS) or S (for SeaWiFS).

BRDFs for higher solar and satellite zenith angles. The Simpson Desert was found to be a suitable area because of its high brightness and location in relatively lower latitudes in the West Pacific longitudinal sector.

We then searched for potential targets in the Simpson Desert. Although analysis was done for all three bands, results are provided only for the surface parameters of MODIS band 1 over the Simpson Desert (Fig. 2). Seven-year (2002–2008) mean brightness, temporal variation, and spatial variation of MODIS band 1 white-sky albedo are shown in Figs. 2a–c, respectively. We also provide the data yielding ratio for MODIS band 1. Analysis results for the NDVI data are not shown because NDVI values were spatially homogenous over most of the Simpson Desert, with mean values less than 0.2. It was difficult to select targets objectively because there was no primary, important parameter. Instead, we subjectively selected targets showing higher brightness, lower spatial and temporal variations, and higher data yield ratio in all three MODIS channel measurements of white-sky albedo. The selected target is shown as a box (25.924°S–26.325°S, 136.925°E–137.425°E) outlined with thick dashed lines. The values for brightness, temporal variation, spatial variation, and yield ratio within the box appeared to be around 0.3, 3%, 5%, and 95%, respectively. We subdivided the selected desert target ($0.5^\circ \times 0.5^\circ$) into sub-targets whose individual size was about $0.05^\circ \times 0.05^\circ$ (about 5 km \times 5 km). The locations of the chosen 10 best targets showing higher brightness as well as lower spatial variability are indicated as small squares in Fig. 2d.

In order to understand the characteristics of the surface parameters over the selected target, the time series of brightness; spatial variations of white-sky albedos derived from MODIS band 1 (640 nm), 2 (860 nm), and 4 (550 nm); and NDVI derived from white-sky albedos at bands 1 and 2 are presented in Fig. 3. The values represent the center point (26.075°S, 137.175°E) of the target. It should be noted that there was a continuous increase in surface brightness over the 7-year period in all three bands. It appears that the increasing trend levels off after 2007. It is not clear what caused such a significant increase in the surface brightness over the analysis period, although a decrease in rainfall and continuous drought after the year 2000 that was widespread over the inner desert area of the Australian continent, including the Simpson Desert (not shown), are thought to be reasons for the increasing trend. In contrast, the seasonal variations in brightness appeared to be less significant.

The spatial variation appeared to be relatively stable throughout the analysis period, largely between 0.04 and 0.06. The NDVI showed no obvious seasonal or interannual trend, except for intermittent sudden increases, as shown in 2003, 2004, and 2005. These sudden increases in NDVI appeared to correspond to sudden decreases in brightness; however, the lack of an obvious trend suggested that the general increase shown in the brightness may not be associated with vegetation changes.

4. Algorithm development

4.1 Surface albedo characterization

In order to use MODIS-derived surface BRDF parameters, surface optical boundary conditions needed to be specified to calculate the TOA radiances measured by other satellite sensors. In doing so, different spectral response functions between the MODIS and other target sensors should be considered (see Fig. 4 for various channel response functions of MODIS, MTSAT-1R, and SeaWiFS). For example, the response function of the MTSAT-1R visible channel in the 500–900-nm spectral range was much broader than any individual MODIS band.

Since calculated TOA radiances were weighted by the channel's spectral response function for comparison with measured radiances, the entire spectral shape of the surface albedo should be specified, at least over the spectral range sensed by the target sensor. To obtain spectral albedo information, the MODIS BRDF parameters at 7 bands were interpolated over the visible and near-infrared spectral range with a 2.5-nm interval by using the ASTER spectral albedo.

Interpolation methodologies are provided schemati-

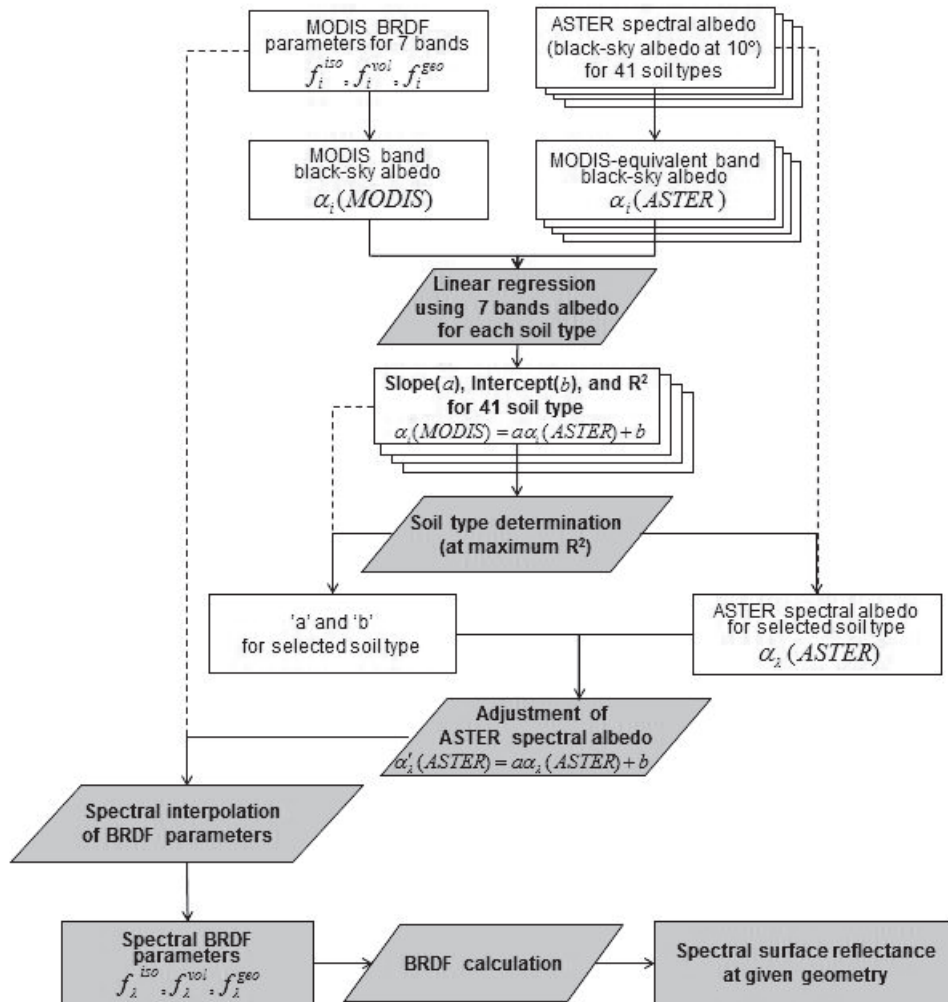


Fig. 5. Schematic diagram of spectral BRDF parameter retrieval. Subscript 'i' is ith MODIS channel, f 's are MODIS BRDF parameters, subscripts (or superscripts) 'iso', 'vol', and 'geo' represent isotropic, volume, and geometric-type scatterings, respectively. Detailed explanation is provided in the text.

cally in Fig. 5. First MODIS-derived black-sky albedo [$\alpha_i(MODIS)$] (MODIS channel number $i = 1, \dots, 7$) was compared with all surface spectra for 41 soil types from the ASTER spectral library in order to determine the soil type most closely matching the MODIS band albedos. Since albedo in the ASTER library represents the surface reflectivity when the light source is located at a zenith angle of 10° (i.e., equivalent to black-sky albedo at 10°), the ASTER-equivalent MODIS black-sky albedo (i.e., $\alpha_i(MODIS)$) was calculated by assuming the sun to be located at 10° of the solar zenith angle

and by integrating BRDFs over the 2π hemisphere. For comparison, the ASTER spectral albedo [$\alpha_\lambda(ASTER)$] was converted into the MODIS-equivalent band albedo [$\alpha_i(MODIS)$] by applying the spectral response function [$RF_{i\lambda}$] of the MODIS sensor provided in Fig. 4, i.e.:

$$\alpha_i(MODIS) = \frac{\sum_{\lambda} \alpha_{\lambda}(ASTER) \times RF_{i\lambda}}{\sum_{\lambda} RF_{i\lambda}}. \quad (2)$$

Table 2. 6S model input variables used for sensitivity test of MTSAT-1R visible channel and obtained results. The TOA reference radiance is associated with reference input conditions, and the required accuracy is the percentage change of an input variable inducing +1% radiance change at the TOA, and expressed as a deviation (given in %) from the reference condition, while other conditions remain fixed.

Input parameters	Reference conditions	Required accuracy (at TOA Radiance: +1%)
O ₃ (DU)	310.0	-100 (~32%)
TPW (g cm ⁻²)	1.5	-0.64 (~43%)
AOT	0.1	-0.05 (~50%)
α _s	0.25	+0.0034 (~1.4%)

For each soil type, α_i(ASTER) was regressed to α_i(MODIS) by minimizing the variance as follows:

$$\text{Min} \left[\sum_{i=1}^7 [a\alpha_i(\text{ASTER}) + b - \alpha_i(\text{MODIS})]^2 \right] \quad (3)$$

where *Min* stands for the minimization, and “*a*” and “*b*” are the adjustment ratio and bias, respectively. Since the 41 soil types have their own explained variances (*R*²) from the regression, one soil type was chosen at maximum *R*². Once the soil type was chosen for the given target and given time, the new ASTER spectral albedo [α'_λ(ASTER)] was calculated by applying *a* and *b* to the original ASTER spectral albedo of the chosen soil type, i.e.,

$$\alpha'_\lambda(\text{ASTER}) = a\alpha_\lambda(\text{ASTER}) + b. \quad (4)$$

Finally, α'_λ(ASTER) was used for calculating the spectral albedo. Since black-sky albedo is linear with BRDF parameters for the given solar zenith angle, the spectral variation of α'_λ(ASTER) is assumed to be expressed by MODIS BRDF parameters such as:

$$\frac{\alpha'_i - \alpha'_\lambda}{\alpha'_j - \alpha'_\lambda} = \frac{f_i^k - f_\lambda^k}{f_j^k - f_\lambda^k} \quad (5)$$

where *i* and *j* are MODIS *i*th and *j*th channel number, respectively; λ is wavelength in interest; and *k* is the type of scattering (i.e. ‘iso’, ‘vol’, or ‘geo’). In so doing, the MODIS BRDF parameters at 7 bands were interpolated to the spectral (2.5-nm interval) wavelength using the spectral variation of α'_λ(ASTER) using Eq. (5), i.e.:

$$f_\lambda^k = f_i^k + \frac{\alpha'_\lambda - \alpha'_i}{\alpha'_j - \alpha'_i} (f_j^k - f_i^k). \quad (6)$$

Then the surface spectral BRDF at given angles (θ, ϑ, φ) was calculated by applying the interpolated

spectral BRDF parameters to the MODIS BRDF model as follows.

$$R_\lambda(\theta, \vartheta, \phi) = f_\lambda^{\text{iso}} + f_\lambda^{\text{vol}} K_{\text{vol}}(\theta, \vartheta, \phi) + f_\lambda^{\text{geo}} K_{\text{geo}}(\theta, \vartheta, \phi). \quad (7)$$

4.2 TOA radiance simulation

As shown in Fig. 1, to simulate the TOA radiance, the calibration algorithm included radiative transfer modeling with specified surface radiative conditions. For the radiative transfer calculation, the Second Simulation of the Satellite Signal in the Solar Spectrum (6S) radiative transfer model (Vermote et al. 1997) was used. Sensitivity tests were conducted to examine how the TOA radiance was affected by the uncertainty level of the input data in the model. TOA radiance calculated from the inputs—total ozone amount = 310 DU, total precipitable water (TPW) = 1.5 g cm⁻², aerosol optical thickness (AOT) = 0.1, surface albedo (α_s) = 0.25—was used as a reference from which the error range induced by uncertain input data was assessed in terms of a relative error in terms of percentages. In this study, we determined the percentage change in an input variable (with other variables fixed) that would cause a 1% change in the TOA radiance.

Sensitivity results are given in Table 2. A 1% error in TOA radiance could be induced by approximately 32% of the total ozone amount, 43% of TPW, or 50% of AOT. On the other hand, the same 1% error could be induced by about 1.4% of surface albedo, indicating that surface albedo was the most important parameter for the simulation. Therefore, accurate surface characterization was a prerequisite for vicarious calibration using a radiative transfer modeling approach.

Because the atmospheric contribution to the TOA radiance was much weaker than the surface contribution over the bright desert target, as shown in the sensitivity test results (Table 2), the atmospheric thermodynamic

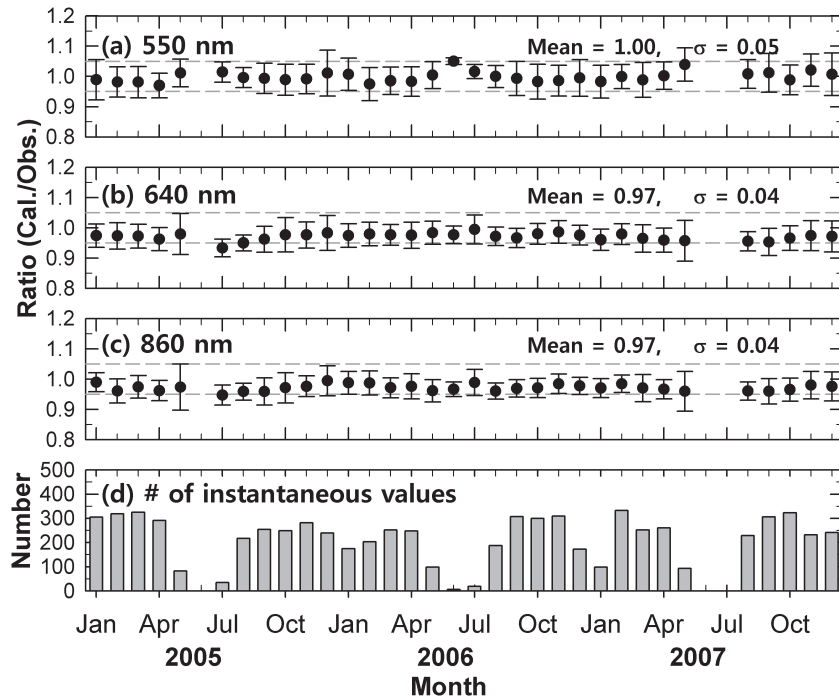


Fig. 6. Time series of monthly mean ratio of calculated radiance to the MODIS-observed value for (a) 550 nm (band 4), (b) 640 nm (band 1), and (c) 860 nm (band 2) channel. The gray dashed lines represent the $\pm 5\%$ error range. The vertical bar at each month represents the range of 1 standard deviation obtained from instantaneous sub-target radiances over the corresponding 1-month period. The bottom panel (d) shows the number of sub-target values used to calculate the monthly statistics. The mean value over the 3-year period (2005–2007) and associated standard deviation calculated from entire instantaneous data for sub-targets are given at the top right of (a), (b), and (c).

conditions were fixed using those for the US standard atmosphere, but adjusted to the OMI total ozone amount and NCEP TPW values. AOT was fixed at 0.1 at 500 nm as a typical value over the selected desert target. As inputs to the 6S model, surface optical properties (i.e., BRDF and white-sky albedo) were specified by using the spectral BRDF parameter introduced in Subsection 4.1. With the specified input conditions, the TOA radiance for a specific satellite sensor could be calculated by taking into account the satellite's geometric parameters and response function.

5. Results

5.1 Validation of the algorithm

The developed algorithm was validated by comparing the simulated TOA radiance with the radiance measured by the reference sensor. We first validated the

data against the Terra MODIS measurements, and then against the SeaWiFS measurements. Because the surface characterization was done with MODIS measurements, validation against the MODIS measurements would be considered to be circular and highly correlated. Another reason to use both satellites was that the sensors in both satellites carry well-performing onboard calibration systems. The onboard radiometric calibration system for the Terra MODIS solar channels consists of a solar diffuser and a solar diffuser stability monitor. In-flight calibration of the MODIS instrument is performed with biweekly solar calibration with a diffuser to achieve radiometric accuracy within 5% for radiance and with regular lunar calibration to monitor radiometric calibration stability (Xiong et al. 2007). In-flight calibration of the SeaWiFS instrument relies on daily solar calibration with a diffuser, monthly lunar calibration,

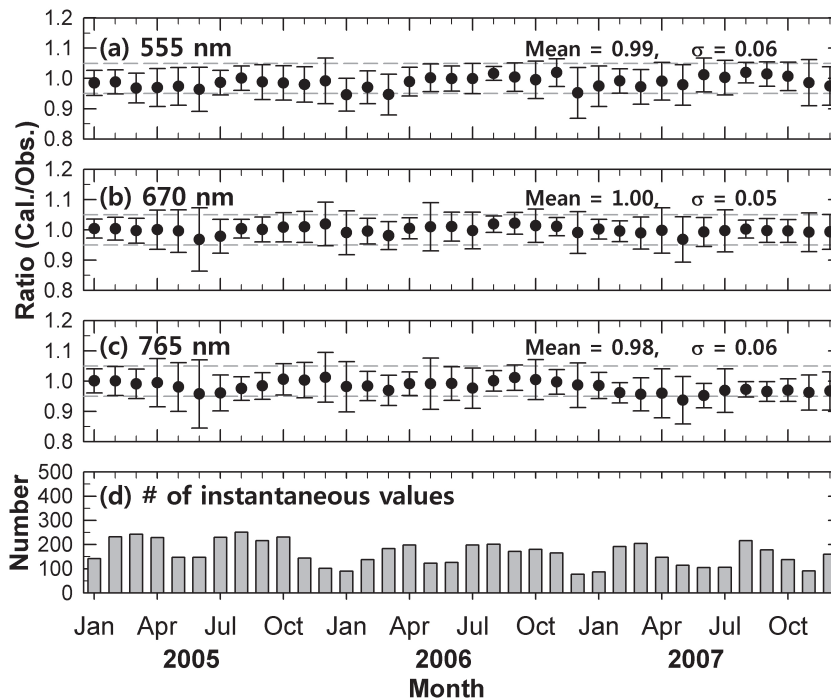


Fig. 7. Same as Fig. 6, except for (a) 555 nm (band 5), (b) 670 nm (band 6), and (c) 765 nm (band 7) of SeaWiFS channels.

and vicarious calibrations to achieve a radiometric accuracy to within 5% for radiance (McClain et al. 2004).

To assess the performance of the developed calibration algorithm, the relative simulation error was obtained by normalizing the simulated radiance with the observed value for a specific time. For example, a 1.05 ratio implies that 5% was overestimated by the algorithm in comparison to the observation. Results are given as a monthly mean for all simulated values at 10 sub-targets, and are given for 3 solar channels (550 nm, 640 nm, and 860 nm). This was done so as to reduce the simulation errors caused by uncertainties associated with instantaneous atmospheric and surface input parameters. To reduce uncertainties from the BRDF calculation, simulation results are excluded from the average if the solar zenith angle is larger than 50°. Also given is the number of sub-targets used for the monthly average.

MODIS simulations results are given in Fig. 6. As shown in the number of data points used for obtaining the monthly mean, the June–July period did not have enough data due to the lower elevation angle of the sun, which leads to larger errors in this period, even if the monthly mean is calculated. Despite weak

seasonal variations, the monthly means of the simulated MODIS radiances generally showed an uncertainty range smaller than 5% compared to observation. The 3-year means (and associated standard deviations) obtained from all available instantaneous radiances for the sub-targets were 1.00 (0.05), 0.97 (0.04), and 0.97 (0.04) for the 550, 640, and 860 nm channels, respectively. Mean biases around 3% were clear for the 640 and 860 nm channels.

However, considering that the surface BRDFs were retrieved from MODIS measurements, validating the developed calibration algorithm against the MODIS-measured radiance would be circular. For this reason, we compared the simulated results against the well-calibrated SeaWiFS measurements. Results for the SeaWiFS 555 nm, 670 nm, and 765 nm channels are given in Fig. 7. It is shown that the data points available during the austral winter were larger than those for MODIS. The equatorial crossing time of around noon for the SeaWiFS is later than 10:30 a.m. for MODIS, resulting in more available data for SeaWiFS at the comparatively higher solar elevation angle. Despite the different sensor and bands, the calculated radiances were

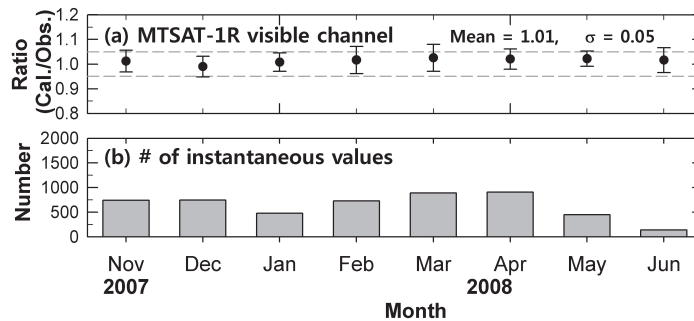


Fig. 8. Same as Fig. 6, except for MTSAT-1R from November 2007 to June 2008.

again mostly within a 5% uncertainty range. The 3-year means (and the associated standard deviations) were 0.99 (0.06), 1.00 (0.05), and 0.98 (0.06) for the 555, 670, and 765 nm channels respectively, showing that the statistics for the SeaWiFS simulations were comparable to those found in the MODIS simulations. Overall, the validation against the SeaWiFS measurements further suggested that the developed algorithm using the selected desert target in Australia could be used to calibrate solar channels within a 5% uncertainty range.

5.2 Application to MTSAT-1R visible channel

We examined the calibration status of the MTSAT-1R visible channel using the desert target under the assumption that the developed method provided calibration accuracy within a 5% uncertainty range. Figure 8 shows the time series of the monthly mean and its associated standard deviation for the simulated MTSAT-1R visible channel radiance divided by the observed radiance from November 2007 to June 2008 and the number of data used for the monthly average. The 8-month mean ratio (1.01) and associated standard deviation (0.05) from all available sub-target data are also provided.

It was demonstrated that the MTSAT-1R visible channel measured the radiance within a 5% uncertainty range. However, as a caveat to this method of using targets in the Simpson Desert, less available data during the austral summer seemed to hamper the calibration capability all year round.

In order to utilize the developed algorithm as a means to calibrate the MTSAT-1R visible channel, it was necessary to convert the digital counts into radiances. The calculated radiance at the sub-target and the corresponding digital count value were plotted for each month (Fig. 9). The digital count value was obtained by taking the average of all available sub-target values. By regressing

the digital count values to simulated radiances, the slope and intercept points were determined, and these values were used as the calibration coefficient and space offset count, respectively. The slope varied from 0.3996 (April 2008) to 0.4390 (January 2008), while the intercept point at the zero count value was also variable from 1.4021 (January 2008) to 8.5566 (March 2008). The range between the minimum and maximum slope within 8 months was within 10%, which was consistent with the uncertainty range of $\pm 5\%$. The obtained slopes were also consistent with the MTSAT-1R results, suggesting that the MTSAT-1R calibration appears to perform within a 5% error range for digital count values smaller than about 350. On the other hand, it is true that different intercepts shown in Fig. 9 have influence on the calibration accuracy. However, considering that the inclusion of offset value in assessing the calibration accuracy would result in the calibration accuracy depending on the count value itself, it may not be appropriate to include the offset value as a part of discussion.

6. Summary and discussion

We developed an algorithm to calibrate the visible sensor aboard a geostationary satellite located over the western Pacific region (MTSAT-1R) using bright desert targets. This method is important because the satellite is not equipped with an on-board calibration system for the visible channel. Although bright targets are preferable for vicarious calibration, the use of desert targets has been rare in the East Asia–West Pacific region.

First, we selected bright, temporally and spatially stable targets using MODIS-derived BDRFs, and then conducted radiative transfer calculations with the specified surface albedo from MODIS measurements in conjunction with spectral albedo from the ASTER library. By adjusting the ASTER spectral albedo values

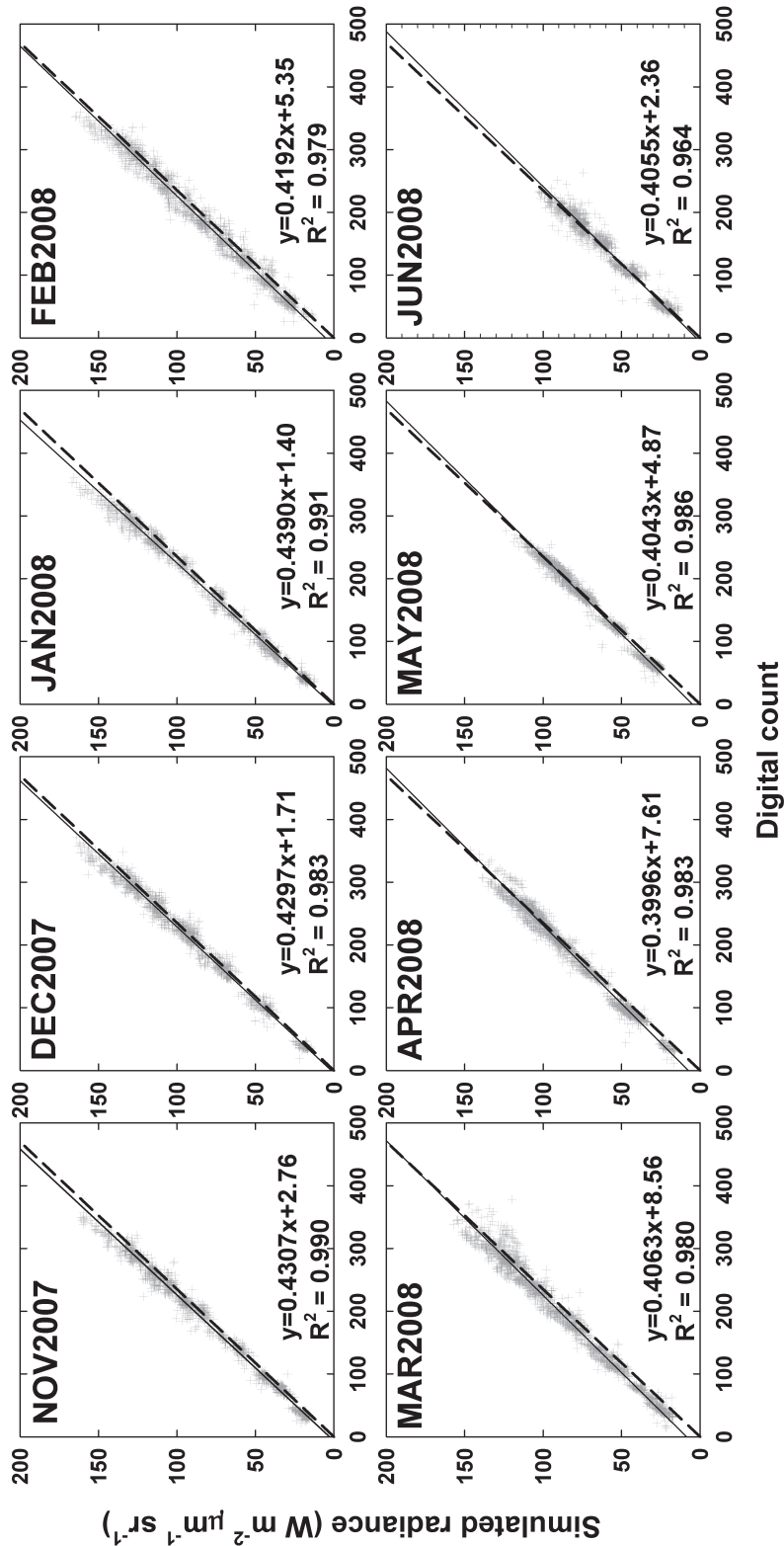


Fig. 9. Scatter plots of simulated TOA radiances for MTSAT-IR visible channel versus the corresponding digital counts. Dashed lines are based on MTSAT-IR operational calibration, and solid lines are from the linear regression. The digital count values for MTSAT-IR are between 0 and 1023.

to MODIS channel albedos, we obtained the spectral BRDFs over the solar spectrum, which was then further used for spectral integration in conjunction with the specific channel response function.

Selected MODIS and SeaWiFS visible channel measurements were simulated over the selected targets. It was shown that the relative errors between calculated and MODIS/SeaWiFS channel radiances were within a $\pm 5\%$ uncertainty range, indicating that the developed calibration method using a desert target over the Australian Simpson Desert could be used to calibrate the geostationary visible channel to within a 5% uncertainty level.

By applying the developed algorithm to MTSAT-1R visible channel measurements, it was found that MTSAT-1R operational (or preflight) calibration for the visible sensor appears to be within a 5% error range. Despite this, we suspect that the current method alone may not be sufficient for MTSAT-1R measurements. Recently, Ham and Sohn (2010) investigated the calibration performance of the MTSAT-1R visible channel using 3 methods: MODIS-based ray matching technique; radiative transfer model using MODIS cloud products as inputs; and deep convective cloud (DCC) method (Sohn et al. 2009). The calibration accuracy of the MTSAT-1R visible channel was found to be variable with the target radiance because of an underestimation of (1) the calibration coefficient (up to 20%) and (2) the positive radiance interception point (Ham and Sohn 2010). The count values under consideration in this study were up to 350 (corresponding to albedo around 30%) in the 0–1023 digital count range. Thus, the calibration algorithm developed in this study, performing within a $\pm 5\%$ error range, should be valid, at least within the lower end of the count range. However, considering that the count values of bright targets such as deep convective clouds are much larger than 350, the desert target approach would not be sufficient for calibration over the entire radiance range of interest. If the calibration coefficient is determined only from a narrow count range, then the associated small error could lead to an incorrect offset account and slope, and thus induce a larger error at the bright end. The combination of a desert target with other methods, such as cloud methods, is more desirable; therefore, any results based solely on the desert target approach should be interpreted with caution.

Acknowledgements

We convey our thanks to two anonymous reviewers for providing helpful comments and suggestions.

Special thanks are given to the editor who carefully read the manuscript and gave many helpful comments which led us to improve the manuscript. Our thanks are also extended to Dr. Eves Govaerts at the European Organisation for the Exploitation of Meteorological Satellites (EUMETSAT) for valuable discussion on the solar channel calibration using desert target, particularly in the beginning of this research. We acknowledge that MODIS data and ASTER spectral library data were from NASA's Distributed Active Archive Center (DAAC) NASA GSFC and the NASA JPL. This work was supported by the Korea Meteorological Administration Research and Development Program under Grant CATER 2006-2103.

References

- Baldrige, A. M., S. J. Hook, C. I. Grove, and G. Rivera, 2009: The ASTER spectral library version 2.0. *Remote Sens. Environ.*, **113**, 711–715.
- Barnes, W. L., T. S. Pagano, and V. V. Salomonson, 1998: Prelaunch characteristics of the Moderate Resolution Imaging Spectroradiometer (MODIS) on EOS-AM1. *IEEE Trans. Geosci. Remote Sens.*, **36**, 1088–1100.
- Cao, C., X. Xiong, A. Wu, and X. Wu, 2008: Assessing the consistency of AVHRR and MODIS L1B reflectance for generating fundamental climate data records. *J. Geophys. Res.*, **113**, D09114, doi:10.1029/2007JD009363.
- Chung, J. Y., H. K. Lee, H. J. Ahn, M. H. Ahn, and S. N. Oh, 2006: Developing the cloud detection algorithm for COMS Meteorological Data Processing System. *Korean J. Remote Sens.*, **22**, 367–372.
- Cosnefroy, H., M. Leroy, and X. Briottet, 1996: Selection and characterization of Saharan and Arabian desert sites for the calibration of optical satellite sensors. *Remote Sens. Environ.*, **58**, 101–114.
- Govaerts, Y. M., and M. Clerici, 2004: Evaluation of radiative transfer simulations over bright desert calibration sites. *IEEE Trans. Geosci. Remote Sens.*, **42**, 176–187.
- Govaerts, Y. M., M. Clerici, and N. Clebaux, 2004: Operational calibration of the Meteosat radiometer VIS band. *IEEE Trans. Geosci. Remote Sens.*, **42**, 1900–1914.
- Ham, S.-H., and B. J. Sohn, 2010: Assessment of the calibration performance of satellite visible channels using cloud targets: application to Meteosat-8/9 and MTSAT-1R. *Atoms. Chem. Phys.*, **10**, 11131–11149.
- Japan Meteorological Agency, 2003: *JMA HRIT mission specific implementation*, Issue 1.2, 59 pp.
- Lucht, W., C. B. Schaaf, and A. H. Strahler, 2000: An algorithm for the retrieval of albedo from space using semiempirical BRDF models. *IEEE Trans. Geosci. Remote Sens.*, **38**, 977–998.
- McClain, C., G. Feldman, and S. Hooker, 2004: An overview of the SeaWiFS project and strategies for producing a climate research quality global ocean bio-optical time

- series. *Deep-Sea Res. Part. II*, **51**, 5–42.
- Miesch, C., F. Cabot, X. Briottet, and P. Henry, 2003: Assimilation method to derive spectral ground reflectance of desert sites from satellite datasets. *Remote Sens. Environ.*, **87**, 359–370.
- Minnis, P., D. R. Doelling, and L. Nguyen, 2008: Assessment of the visible channel calibrations of the VIRS on TRMM and MODIS on Aqua and Terra. *J. Atmos. Oceanic. Technol.*, **25**, 385–400.
- Mitchell, R. M., D. M. O'Brien, M. Edwards, C. C. Elsum, and R. D. Graetz, 1997: Selection and initial characterization of bright calibration site in the Strzelecki desert, South Australia. *Can. J. Remote Sens.*, **23**, 342–353.
- Sohn, B. J., S.-H. Ham, and P. Yang, 2009: Possibility of the visible-channel calibration using deep convective clouds overshooting the TTL. *J. Appl. Meteor. Climatol.*, **48**, 2271–2283.
- Teillet, P. M., G. Fedosejevs, K. J. Thome, and J. L. Barker, 2007: Impacts of spectral band difference effects on radiometric cross-calibration between satellite sensors in the solar-reflective spectral domain. *Remote Sens. Environ.*, **110**, 393–409.
- Vermote, E. F., and N. Z. Saleous, 2006: Calibration of NOAA16 AVHRR over a desert site using MODIS data. *Remote Sens. Environ.*, **105**, 214–220.
- Vermote, E. F., D. Tanre, J. L. Deuze, M. Herman, and J. J. Morcrette, 1997: Second simulation of the satellite signal in the solar spectrum, 6S: An overview. *IEEE Trans. Geosci. Remote Sens.*, **35**, 675–686.
- Xiong, X., and W. Barnes, 2003: Early on-orbit calibration results from Aqua MODIS. *Sensors, Systems, and Next-Generation Satellites VI* [ed. H. Fujisada et al., International Society for Optical Engineering], SPIE Proc., **4881**, 327–336.
- Xiong, X., J. Sun, W. Barnes, V. Salomonson, J. Esposito, H. Erives, and B. Guether, 2007: Multiyear on-orbit calibration and performance of Terra MODIS reflective solar bands. *IEEE Trans. Geosci. Remote Sens.*, **45**, 879–889.